

International Conference on Space Optics—ICSO 2022

Dubrovnik, Croatia

3–7 October 2022

Edited by Kyriaki Minoglou, Nikos Karafolas, and Bruno Cugny,



Sampling Strategies for Rotating Synthetic Aperture Space Telescopes



Sampling Strategies for Rotating Synthetic Aperture Space Telescopes

Evan L. Kramer^a, Joseph J. Green^b, Rebecca A. Masterson^a, and David W. Miller^a

^aMIT, 77 Massachusetts Ave, Cambridge, MA, USA

^bNASA JPL, 4800 Oak Grove Dr, Pasadena, CA, USA

ABSTRACT

Optical imagery from space-based telescopes is one of the most valuable tools for understanding various large and small-scale processes on planetary bodies. Whether in orbit around the Earth or another body in the solar system, it is desirable to obtain the highest resolution imagery possible of the central body. The traditional approach to achieving higher resolution imagery is to increase the size of the optical payload's aperture. However, larger aperture payloads become prohibitively difficult to manufacture and excessively expensive to design, build, launch, and operate. Application of rotating synthetic apertures (RSA), which is a form of dilute aperture imaging system, to space telescope designs have the potential to unlock the design space of low mass and cost, high resolution space telescopes. RSAs employ a high aspect ratio rectangular aperture that is spun about its principal optical axis. A complete image is formed after a 180° rotation during which multiple frames are acquired to fully sample the imaging system's optical transfer function. The sampling strategy, which involves the number of individual frames captured and the rate of spin about the principal optical axis, is a function of the RSA's aperture dimensions.

The purpose of this work is twofold. First, an expression for resolution in reconstructed images is derived as a function of orbital altitude, RSA aperture dimensions, and amount of spatial oversampling of the target scene. This expression is used to predict potential science data return for a given orbit, RSA design, and sampling strategy. Second, a multi-objective optimization analysis is performed between reconstructed image resolution and optical telescope assembly (OTA) cost from which a Pareto frontier is defined. This analysis informs an ensuing discussion of optimal RSA aperture dimensions for achieving optimal conditions in resolution and cost. Additionally, the effects of different RSA aperture dimensions on sampling strategies are discussed. Based on these results and discussions, a high-level design for an RSA demonstration mission is proposed.

Keywords: Manuscript format, template, SPIE Proceedings, LaTeX

1. INTRODUCTION

1.1 Rotating Synthetic Aperture Technology

Whether ground-based or space-based, a telescope's ability to resolve fine details in the imaged scene is a function of its light collecting ability. The root of this dependency can be traced back to the Rayleigh Criterion, which for a diffraction limited system with a circular aperture, relates angular resolution to aperture diameter and wavelength as shown in Equation 1.

$$\theta \approx 1.22 \frac{\lambda}{D} \quad (1)$$

The angular resolution of the imaging system is given by θ , the wavelength of light is λ , and the diameter of the imaging payload's aperture is D . To achieve better imaging resolutions, the goal is to minimize θ , which ultimately translates into the need to maximize D . Traditional telescopes have light collecting areas that are circular in shape while some modern designs, including the James Webb Space Telescope, use segmented optics to approximate circular apertures.¹ Both traditional circular apertures and the more modern segmented designs are forms of filled aperture imaging systems, or imagers that sample the entire frequency space of the object

Evan L. Kramer: E-mail: ekramer3@mit.edu, Telephone: 1 703 340 7525

scene in a single observation. Dilute aperture imaging systems sample the frequency space of the object scene through a sequence of observations. Typically, either the imaging system or target is reoriented between captures to introduce new portions of the target scene into the payload's field of view (FOV). Application of image post processing algorithms to the sequence of captured images can reconstruct the complete image that would have been captured by the filled aperture system. At its core, rotating synthetic aperture (RSA) technology is an application of dilute aperture imagery to spacecraft design. Figure 1 shows a CAD rendering of a cubesat-scale RSA.



Figure 1. CAD rendering of a cubesat-scale RSA.²

Given the requirement of dilute aperture systems to take a sequence of images with different relative perspectives to fully sample the object scene frequency space, the concept of operations (CONOPS) of an RSA space telescope is different from the CONOPS of filled aperture designs. RSA telescopes operate by pointing the principal optical axis at a target and tracking said target for the full duration of an observation. While tracking, the telescope rotates its rectangular aperture about the optical axis at a precisely controlled rate. Images are captured throughout the rotation. An observation maneuver is completed once the full spatial frequency content of the object scene is captured. In the case of a rectangular strip mirror, a 180° rotation is required to complete an observation.

RSAs have the potential to unlock the design space of extremely high spatial resolutions and high temporal frequencies without incurring significant mass and cost barriers. As discussed previously, RSAs are capable of producing complete images with angular resolutions equal to, and in some cases, better than those captured by circular aperture systems 2.1. This performance improvement is achieved while reducing the payload's light collecting area by nearly a factor of eight. RSAs have the potential to become the next revolutionary design for space-based observing systems.

2. BACKGROUND

2.1 Factors impacting image resolution

To determine the theoretical best resolution of an imaging system, aberrations including defocus and distortion are overlooked to presume a perfect optical system. In doing so, the system's limiting resolution becomes a function of just the physical behavior of light as it interacts with optical elements. Diffraction describes the deviation of light from rectilinear propagation. The laws of diffraction differ depending on the distance between

the source and observation points from the diffracting element. When distances are small, near-field, or Fresnel diffraction takes place. However, since our focus is on space telescope applications, a special case of Fresnel diffraction called far-field, or Fraunhofer diffraction, is considered.

The conditional assumption of the Fraunhofer diffraction formula is that the Fraunhofer condition is met. This condition can be understood by considering figure 2 which shows the annotated geometry for a line of point sources and an observation point P . The Fraunhofer condition requires the lengths r_i to be linear with respect to

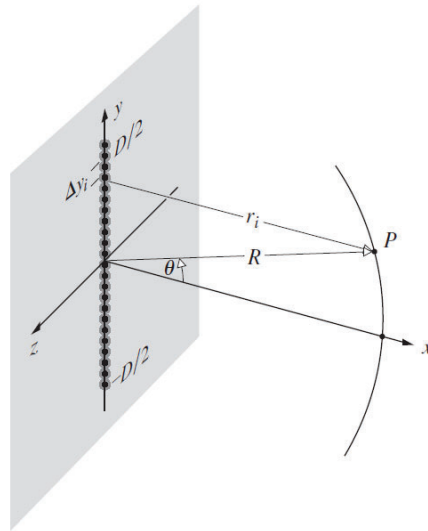


Figure 2. Annotated geometry for a line of length D of point sources and an observation point P .³

the dimensions of the diffracting element. This requirement reduces the sensitivity of the diffracted wavefront to the phase component containing r_i . Writing r_i in terms of the y coordinate using a Maclaurin series expansion, we obtain equation 2.

$$r_i = R - y_i \sin(\theta) + (y_i^2/2R) \cos(\theta)^2 \quad (2)$$

The nonlinear term in equation 2 can be considered negligible when R is very large. This implies that the distances from the source and observation points to the diffracting element must be large, hence the terminology "far-field" diffraction. While there is no particular distance for determining the necessary value of R for this assumption to hold, a practical rule of thumb is given in equation 3.

$$R > \frac{a^2}{\lambda^2} \quad (3)$$

R represents the smaller of the two distances from source and observation point to the diffracting element, a is the greatest width of the diffracting element, and λ is the source wavelength. In the case of a space telescope, the distance from target source to aperture can be considered to be ∞ . However, the distance from the telescope aperture to the observation plane of the instrument is often on the order of 1-10m and does not strictly meet the condition in equation 3. Nevertheless, in the context of the RSAs considered in this work, the Fraunhofer diffraction formula will still produce results that are accurate to the first order.³ An additional note is that strategic placement of lenses or shaped mirrors within the imaging instrument can collimate light from the other diffractive optical elements onto the detector causing R to appear to be ∞ as shown in figure 3.

The theoretical best imaging resolution of an optical system is defined in terms of the ability to resolve adjacent peaks in the irradiance distribution at the image plane. Most imaging systems have circularly-shaped apertures. Equation 4 provides the normalized irradiance distribution for a circular aperture as a function of

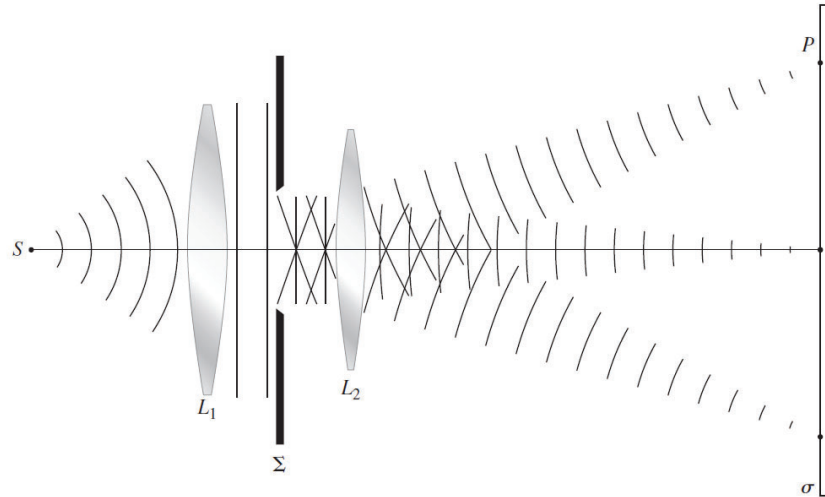


Figure 3. L1 is used to collimate light from source S so it appears to be coming from ∞ . L2 is used to focus the various angular frequencies of diffracted light to points on the image plane at P and σ . In this manner, L2 acts as a Fourier transform of the diffracted light.³

angular separation, θ .

$$I(\theta)/I(0) = \left[\frac{2J_1(ka \sin \theta)}{ka \sin \theta} \right]^2 \quad (4)$$

The irradiance distribution is normalized by dividing by the irradiance at the center of the pattern, $I(0)$. The radius of the aperture diameter is a and the wavenumber is $k = 2\pi/\lambda$. The first order Bessel function, J_1 , is evaluated at the quantity $ka \sin \theta$ for a range of θ . Figure 4 plots the irradiance distribution for a circular aperture with radius of 35cm as a function of angular distance.

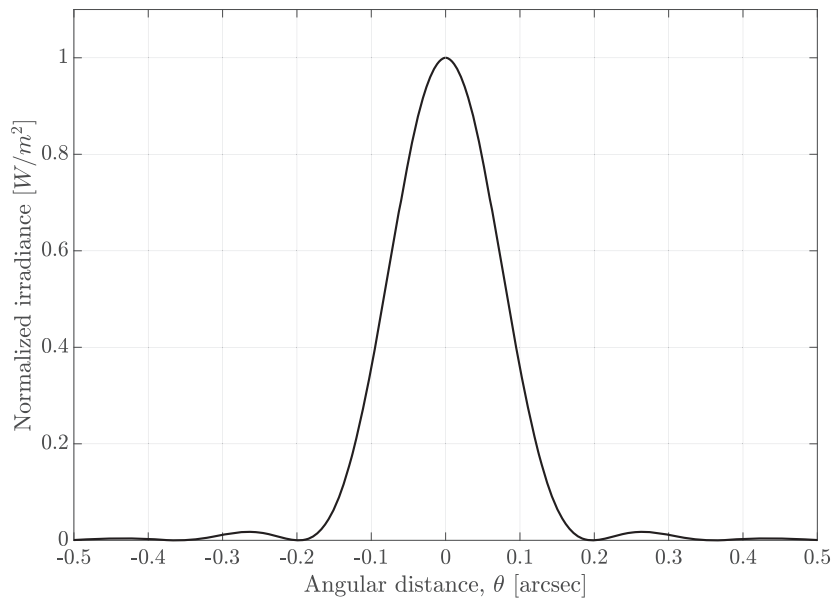


Figure 4. Irradiance distribution for circular aperture.

For a rectangular-shaped aperture, the normalized irradiance distribution is described by equation 5.

$$I(\theta)/I(0) = \left(\frac{\sin \alpha'}{\alpha'} \right)^2 \left(\frac{\sin \beta'}{\beta'} \right)^2 \quad (5)$$

With Y and X representing Cartesian coordinates in the image plane, a representing the length dimension of the rectangular aperture, b representing the width dimension of the rectangular aperture, and R representing the distance from the diffracting element to the image plane, $\alpha' = kaX/2R$ and $\beta' = kbY/2R$. A symmetric

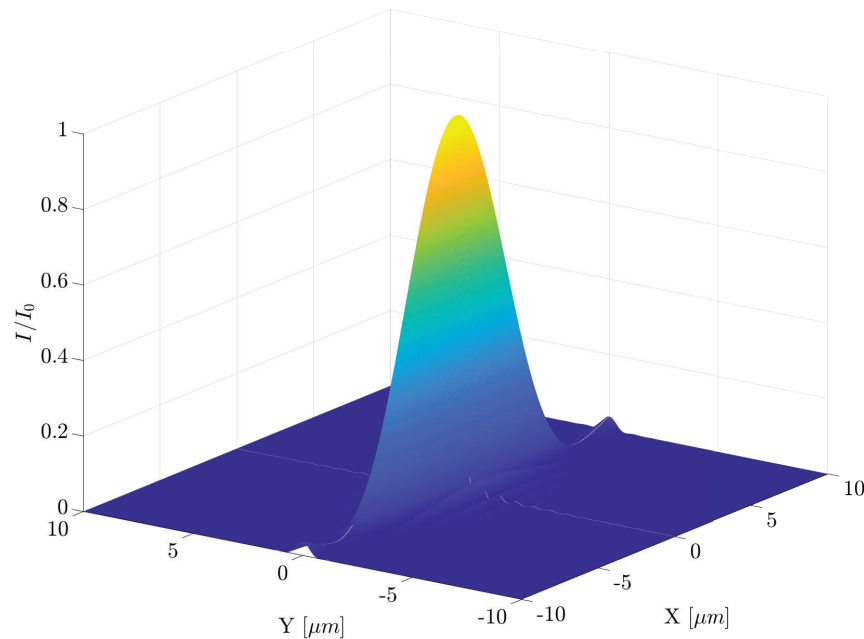


Figure 5. Irradiance distribution for rectangular aperture.

irradiance distribution is produced when $a = b$. However, for a 10: 1 aspect ratio RSA mirror as the diffracting element, the irradiance distribution is elongated along the width (X) axis as shown in figure 5.

For axially symmetric irradiance distributions, an Airy disk describes the central maximum and lower order ripple patterns. Each dark ring in the Airy disk corresponds to a zero in the first order Bessel function J_1 . There are a variety of criterion that exist for quantifying the theoretical best imaging resolution of an optical system based on the irradiance distribution. Consider two point sources of light that are being imaged by an optical device onto an image plane. One of the most popular resolving criterion is the Rayleigh criterion, which states that the point sources are just resolved when the center of one Airy disk falls on the first minimum of the second Airy disk. The familiar expression for angular resolution for circular aperture optical systems given in equation 1 is the angular distance for which the Rayleigh criterion is satisfied. The lack of axial symmetry in the irradiance distribution for an RSA shown in figure 5 implies that equation 1 is not the appropriate definition for angular resolution. Instead, the length dimension of the mirror has a higher angular resolution than the width dimension. The higher resolution along the length dimension is considered as the maximum resolution of the corresponding RSA in this work. This assumption is made on the basis that the filled image that is obtained after multi frame image registration is the data product of interest with an angular resolution equal to that of the high resolution dimension of the RSA.

While the optical components of an imaging system limit the amount of information transferred from the scene to the focal plane array (FPA), the characteristics of the image sensor also play a role in defining the

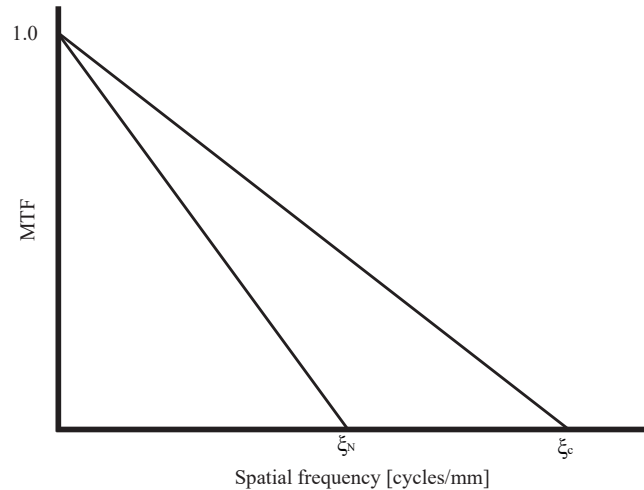


Figure 6. MTF curves for an imaging system's optics and detector. This system is detector-limited corresponding to a $Q < 2$ system.

maximum image resolution. The Q factor quantifies the ratio of the maximum spatial frequency resolveable by the optics to the maximum sampling frequency set by the sensor as defined in equation 6.

$$Q = \frac{2\xi_N}{\xi_C} \quad (6)$$

The detector sampling frequency is $\xi_N = 1/p$ and the cutoff frequency for a circular aperture imaging system is $\xi_C = 1/[\lambda(f/D)]$.⁴ The maximum spatial frequency of the optics is called the optical cutoff frequency and corresponds to the $y=0$ point of the imaging system MTF curve as shown in figure 6. A typical rule of thumb is to sample the information presented to the FPA at the Nyquist frequency, or at $Q = 2$, where the best spatial frequency coverage is obtained between detector and optics without ambiguity. Q values less than 2 result in aliased Fourier domain components resulting in information loss. However, for RSAs, intentional clocking of the primary mirror relative to the FPA can avoid overlap of the image spectrum in the Fourier domain for designs with $Q < 2$. A detailed Fourier domain analysis for RSAs is out of the scope of this paper. However, non-overlapping spectra in the Fourier domain enables restoration of the filled image to the imaging system's cutoff frequency. Additionally, low Q systems have fewer pixels across a target than high Q systems resulting in more relaxed integration time requirements.⁵

Given that the final data product of interest is the filled image obtained after multi frame registration, an additional aspect that would effect RSA image resolution is the amount of overlap present in consecutive image frames captured during an observation. The regions of the target scene that are overlapped are sampled at slightly different object points enabling the use of multi frame super resolution algorithms. Super resolution algorithms reconstruct spatial frequency content beyond the cutoff frequency of the imaging system. The resolution in the overlapping regions scales with the number of images captured. However, the improvement in resolution plateaus as more images are captured.⁶ While many multi frame super resolution algorithms exist, literature focused on determining the upper bound for resolution improvement suggest an improvement of 1.6X the system cutoff frequency is possible.⁷

2.2 Cost modeling

Some of the earliest cost models for telescopes were produced by the prominent astronomer and optical scientist Aden Meinel.⁸ Meinel surveyed the costs and aperture sizes of a variety of optical and radio ground-based telescopes in the late 1970s and early 1980s. Even in these early works, Meinel appreciated the importance of relating the cost of a telescope to its primary aperture size, which is a principal design driver. Meinel made an important distinction in the specific cost referenced for each design. Instead of using total program cost, which

depended on telescope location and various sources of overhead, the cost of the telescope hardware alone was related to aperture diameter. Meinel’s scaling law evolved from a $D^{2.0}$ to a $D^{2.7}$ relationship as more data points were incorporated into the data set and more accurate cost and aperture data were made available.^{8–10} While Meinel’s models can successfully predict cost to the first order, its application should be limited to the scope of ground-based telescopes. This is due to the fact that an entirely unique set of engineering design challenges exist for space-based telescopes that are not present for ground-based designs. As a result, a new set of models have been created that include space-based telescope data that reference the relation between aperture diameter and cost in Meinel’s early cost model.

More recent works by NASA Marshall Spaceflight Center senior optical scientist Philip H Stahl are based on data collected on both ground and space-based telescopes. A multivariable parametric cost model for both ground and space-based telescopes was developed by considering a set of cost estimating relationships (CERs) that predict optical telescope assembly (OTA) cost and are not correlated with one another. Stahl’s most recent work establishes the most current version of the cost model.¹¹ Stahl’s cost model is given in equation 7.

$$OTA\$(FY17) = \$20M \times 30^{S/G} \times D^{1.7} \times \lambda^{-0.5} \times T^{-0.25} \times e^{-0.028(Y-1960)} \quad (7)$$

The S/G parameter specifies whether the model is for ground-based or space-based telescopes by specifying a 0 or 1 respectively. The D parameter corresponds to the telescope primary aperture diameter, λ refers to the diffraction limited wavelength of the optical system, T is the OTA operating temperature, and Y is the current year. This model assume a circular shape for the telescope’s primary aperture. To put the OTA cost in context of the more general project cost, Stahl showed that the OTA accounts for just 10%-15% of the total cost of astronomical telescopes. Nevertheless, a nearly five-fold cost savings on a subsystem that accounts for 10%-15% of the total cost of a project has the potential to save millions of dollars.

2.3 Modeling RSA dynamics

The torque on a rigid body that is rotating with respect to an inertial frame and is undergoing no external disturbance torques is given in equation 8.

$$\boldsymbol{\tau}^B = I\dot{\boldsymbol{\omega}}^B + {}^I\boldsymbol{\omega}^B \times (I\boldsymbol{\omega}^B) \quad (8)$$

The spacecraft moment of inertia (MoI) tensor is denoted as I , the angular velocity vector in the body frame is denoted as $\boldsymbol{\omega}^B$, and the torque in the body frame is denoted as $\boldsymbol{\tau}^B$. The total required momentum exchange for a particular body with known mass and geometry properties is defined as the minimum amount of cumulative torque required to execute a given reference trajectory over time. Deviation from the reference trajectory will always occur regardless of the implemented control algorithm. Nevertheless, required momentum exchange can serve as minimum requirements for spacecraft ADCS. This work is focused on quantifying variations in required momentum exchange for RSA imaging maneuvers as a function of RSA aperture dimensions and spin rates. Therefore, the orbit and imaging target were kept constant for all test cases.

The inertia tensor of a rigid body is a 3x3 matrix that describes its mass and geometry properties. For rigid body dynamics, it describes the torque needed for a desired angular acceleration about a certain rotation axis. Unconstrained three rotational degrees of freedom about the body axes are considered in this work for modeling RSA dynamics. The inertia tensor is constructed relative to a set of principal axes about which torques act independently from one another. Figure 7 shows a simple mass model created in Solidworks of an RSA spacecraft with body axes annotated. The RSA body frame is defined with its origin at the center of mass (CoM), the z-axis pointing along the principal optical axis, the y-axis along the length of the strip mirror, and the x-axis completing a right-handed coordinate frame.

Assuming the RSA rigid body can be modeled as three rectangular prisms, the inertia tensor of the RSA mass model can be computed analytically. Since the MoI tensor of interest is about the system’s CoM, the system CoM must be computed first. Equation 9 describes how the system CoM was computed relative to an inertial coordinate frame, I , with origin located on the back face of the RSA bus at the intersection point of the RSA’s

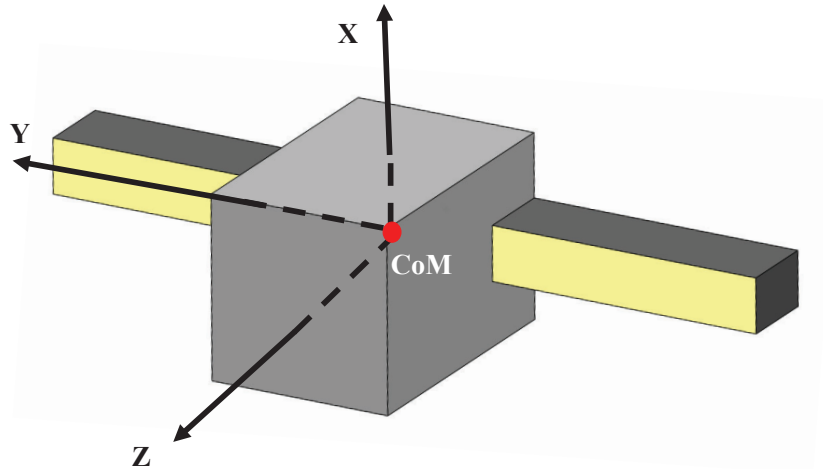


Figure 7. RSA mass model used to obtain a moment of inertia tensor for various RSA aperture and AR dimensions.

YZ and XZ planes of symmetry.

$$\begin{bmatrix} x_{CoM,sys} \\ y_{CoM,sys} \\ z_{CoM,sys} \end{bmatrix} = \begin{bmatrix} \frac{m_1 x_{CoM,1} + m_2 x_{CoM,2} + m_3 x_{CoM,3}}{m_1 m_2 m_3} \\ \frac{m_1 y_{CoM,1} + m_2 y_{CoM,2} + m_3 y_{CoM,3}}{m_1 m_2 m_3} \\ \frac{m_1 z_{CoM,1} + m_2 z_{CoM,2} + m_3 z_{CoM,3}}{m_1 m_2 m_3} \end{bmatrix} \quad (9)$$

Subscript 1 corresponds to the rectangular prism representing the RSA bus, 2 represents the right hand mirror, and 3 represents the left hand mirror. The CoM of the components are easily determined by inspection using symmetry. The mass of each component was computed by multiplying the assigned material density by the component volume. Beryllium with a density of $1,850 \text{ kg/m}^3$ was assigned to the mirrors while T6061 aluminum with a density of $2,700 \text{ kg/m}^3$ was assigned to the spacecraft bus.

The parallel axis theorem was used to calculate the MoI about the system CoM. Equation 10 describes the MoI tensor for each component about the respective component CoM with m_i corresponding to the component mass, W_i is the component width, H_i is the component height, and L_i is the component length.

$$I_{RPi} = \begin{bmatrix} \frac{1}{12} m_i (W_i^2 + H_i^2) & 0 & 0 \\ 0 & \frac{1}{12} m_i (L_i^2 + H_i^2) & 0 \\ 0 & 0 & \frac{1}{12} m_i (L_i^2 + W_i^2) \end{bmatrix} \quad (10)$$

Equation 11 describes the MoI tensor of each component about the system CoM with $X, Y,$ and Z corresponding to the distance between component and system CoM.

$$I_{RPi,CoM} = \begin{bmatrix} I_{RPi,11} + m_i(Y^2 + Z^2) & I_{RPi,12} - m_i(XY) & I_{RPi,13} - m_i(XZ) \\ I_{RPi,21} - m_i(XY) & I_{RPi,22} + m_i(X^2 + Z^2) & I_{RPi,23} - m_i(YZ) \\ I_{RPi,31} - m_i(XZ) & I_{RPi,32} - m_i(YZ) & I_{RPi,33} + m_i(X^2 + Y^2) \end{bmatrix} \quad (11)$$

The system MoI tensor was computed as the summation of the component MoIs about the system CoM. The inertia tensor for a circular aperture mass model was computed in a similar manner with the exception that the mirror component MoI was computed for a solid cylinder as shown in equation 12.

$$I_{cyl} = \begin{bmatrix} \frac{1}{12} m_{cyl} (3R_{cyl}^2 + W_{cyl}^2) & 0 & 0 \\ 0 & \frac{1}{2} m_{cyl} R_{cyl}^2 & 0 \\ 0 & 0 & \frac{1}{12} m_{cyl} (3R_{cyl}^2 + W_{cyl}^2) \end{bmatrix} \quad (12)$$

The radius of the cylinder is R_{cyl} . A central portion of the cylinder was removed by subtracting the MoI of a rectangular prism such that the cylindrical mirror fit around the spacecraft bus without any conflicting intersections.

3. OBJECTIVE FUNCTION DEFINITION

As mentioned in the abstract of this paper, synthesized image resolution and OTA cost are two metrics used to assess the performance of various telescope designs. While obtaining a set of optimal designs for RSAs based on these two metrics is a goal of this work, comparison of RSA designs to more traditional circular apertures is also sought. An additional metric that is particularly informative for this comparison is the total amount of angular momentum exchanged during an observation maneuver. While RSA designs have less mass compared to circular aperture designs, the spinning dynamics required for their observation maneuvers may strain ADCS momentum exchange requirements more than circular aperture designs. Therefore, in order to determine a set of optimal aperture sizes for RSAs, a multi objective optimization algorithm is executed for three objective functions. The set of optimal aperture sizes can be used as an informed design point of departure for RSA demonstration mission designs.

3.1 Resolution objective function

The first objective function pertains to the resolution of the synthesized image produced by an RSA. Several assumptions were made when constructing the resolution objective function. It was assumed that image sequences are registered and synthesized perfectly without any artifacts, the optical system is free of aberrations, and the optical cutoff frequency of the synthesized data product is equivalent to that of a circular aperture system. With these assumptions in mind, the image resolution of an Earth-observing RSA is given in equation 13.

$$GSD = \left(\sqrt{(R_e + h)^2 - R_e^2 \cos^2 \theta_{elv}} - R_e \sin \theta_{elv} \right) \sqrt{\Delta_x \Delta_y / \sin \theta_{elv}} (2f/Q)^{-1} \quad (13)$$

The CMV20000 focal plane array was used as the detector in this work. The CMV20000 is a global shutter CMOS detector that has been used in several imaging instruments on spacecraft including the Mars 2020 Perseverance Rover's engineering cameras and the Orbiting Carbon Observatory 3 context cameras.^{12,13} The CMV20000 has a square pixel pitch of $\Delta_x = \Delta_y = 6.4 \mu\text{m}/\text{px}$ and a focal length of 0.5m was used for all test cases. While the radius of the Earth, R_e , and the orbital altitude, h , remain constant, the elevation angle, θ_{elv} varies. It is common for science requirements to set a threshold for the minimum elevation angle required before image acquisition can begin. For this work, a minimum elevation angle of 40° was specified. The image resolution is minimized when the spacecraft is nadir pointing.¹⁴ While an RSA will capture a sequence of images over different elevation angles, the nadir pointing image resolution was used in this design optimization study. Figure 8 shows a plot of the RSA synthesized and circular aperture image resolution as a function of aperture diameter for a spacecraft in a 300km altitude circular orbit.

3.2 Cost objective function

Stahl's cost model given in equation 7 predicts the cost of an OTA using several parameters, one of which is the telescope diameter. The diameter term in Stahl's model assumes a circular aperture shape and can therefore be related to aperture area. While the length dimension of an RSA can be thought of as the equivalent dimension to a circular aperture's diameter, the area of an RSA's mirror is significantly less than the area of a circular mirror. To account for this areal difference, the diameter of a circular aperture corresponding to the area of the RSA mirror under consideration was computed as shown in equation 14.

$$D_{circ,equiv} = 2\sqrt{A_{RSA}/\pi} \quad (14)$$

The RSA area for a given AR and diameter is computed as $A_{RSA} = D^2/AR$. Aperture diameters from 0.2m to 2.0 meters along with ARs of 5 : 1, 10 : 1, and 20 : 1 were considered in this work. The remaining terms in Stahl's model were defined as $S/G = 1$, $\lambda = 0.5 \mu\text{m}$, $T = 273\text{K}$, and $Y = 2017$ and kept constant throughout all test cases. Figure 9 shows a plot of Stahl's cost model for a traditional circular aperture and an RSA using the equivalent diameter in equation 14 as a function of aperture diameter.

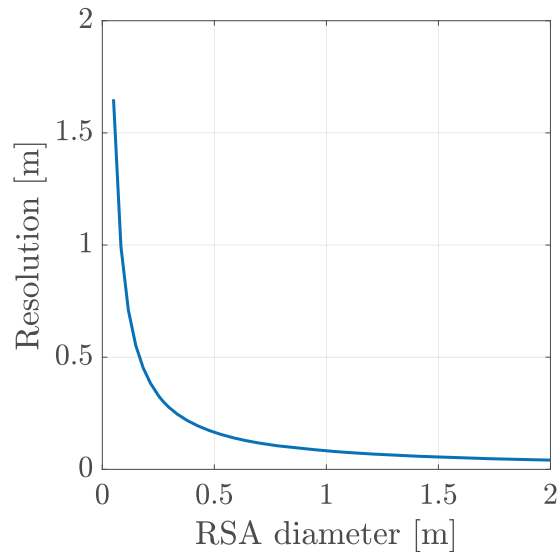


Figure 8. Image resolution as a function of aperture diameter in a 300km altitude circular orbit.

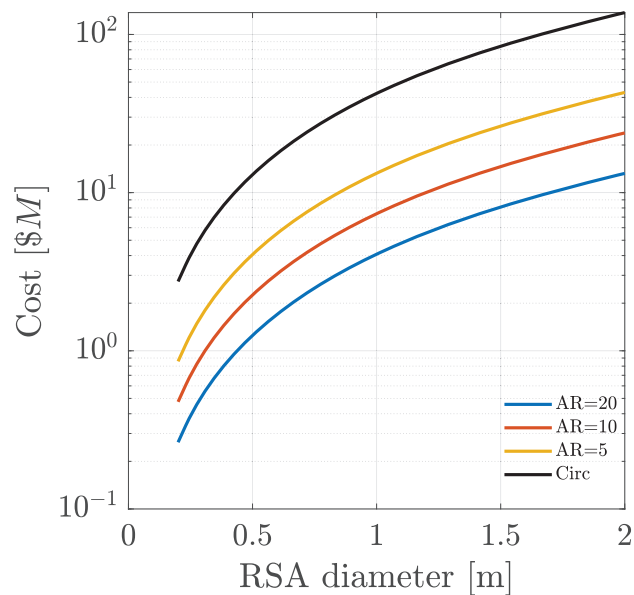


Figure 9. OTA cost as a function of aperture diameter.

3.3 Angular momentum objective function

The third objective function is the total angular momentum exchange required for an imaging maneuver. In order to compute this quantity, Systems Tool Kit (STK) from Analytical Graphics Inc. (AGI) was used to propagate a spacecraft in a 300km altitude low Earth orbit. A single observing target was defined and the orbit was defined such that the spacecraft passes directly overhead. The spacecraft's attitude profile was defined such that its body frame z-axis pointed at and tracked the target point throughout the imaging maneuver over elevation angles from $\pm 40^\circ$.¹⁴

In order to compute the total angular momentum exchange, the torque profile as a function of time must be computed. As shown in equation 8, the angular velocity and acceleration profiles of the spacecraft must be known. In order to obtain these profiles, the spacecraft attitude was recorded from the STK simulation and

differentiated over the duration of the observation maneuver from elevation angles $\pm 40^\circ$.¹⁵ Figure 10 shows the quaternion profile and angular velocity of the simulated spacecraft. The angular velocity was differentiated using

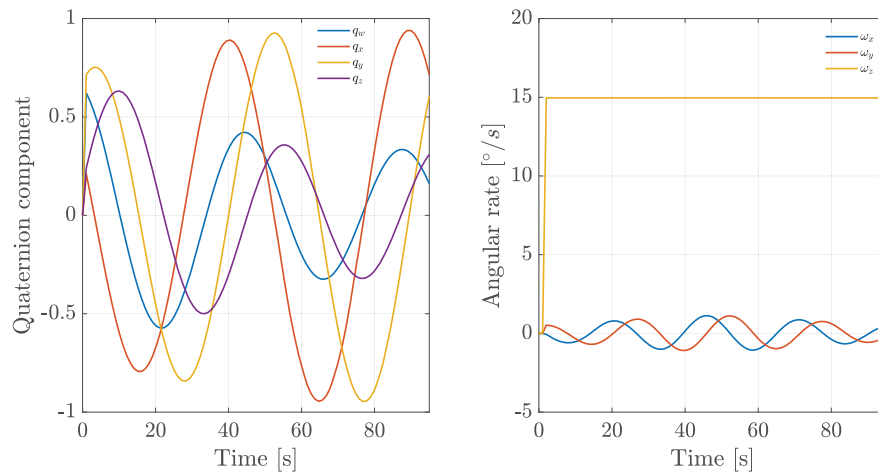


Figure 10. Quaternion and angular velocity profiles for a spacecraft in a 300km altitude orbit performing a target tracking maneuver over elevation angles $\pm 40^\circ$.

the discrete definition of the derivative as shown in equation 15.

$$\dot{\omega}(t) = \frac{\omega(t) - \omega(t - \Delta t)}{\Delta t} \quad (15)$$

Torque profiles were computed according to equation 8. The magnitude of the torque was then computed. Given the relation between angular momentum and torque shown in equation 16, a trapezoidal sum was used to approximate the magnitude of the total angular momentum exchange over the imaging maneuver.

$$|\vec{h}| = \sum_{i=0}^N |\vec{\tau}(\Delta t \cdot i)| \Delta t \quad (16)$$

Figure 11 shows plots of total angular momentum exchange as a function of aperture diameter for the three ARs considered. RSA spin rates from $5^\circ/s$ to $20^\circ/s$ were considered. For a detailed discussion on spin rate ranges for Earth-orbiting RSAs, see.¹⁴

4. PARETO FRONTIER DETERMINATION

The Global Optimization Toolbox in Matlab was used to create a set of solutions that abide by the Pareto optimality condition. This condition states that no improvement to a single objective function can be made without at least one other objective function producing a less desirable value. Specifically, the genetic algorithm was used to produce the Pareto optimal solution set. The genetic algorithm was used due to its ability to optimize nonlinear functions and its ability to avoid converging to local minima solutions as opposed to the global minimum. Generally, the genetic algorithm finds global minimum based on natural selection processes observed in biological evolution. The processes of selection, or retaining a solution that has the best performance of its set, crossover, or creation of new solutions with similarities to previous well-performing solutions, and mutation, or randomly manipulating previous solution parameters to avoid converging to local minimum, form the process framework for the genetic algorithm.¹⁶

Aperture diameter was the sole parameter to be optimized. A bound constraint of 0.2m to 2m was set for aperture diameter and a population size of 200 was set to reduce the likelihood of converging to a local minimum. Each of the objective functions were weighted equally. All other algorithm options were left as the default settings which are described in the toolbox documentation.¹⁶

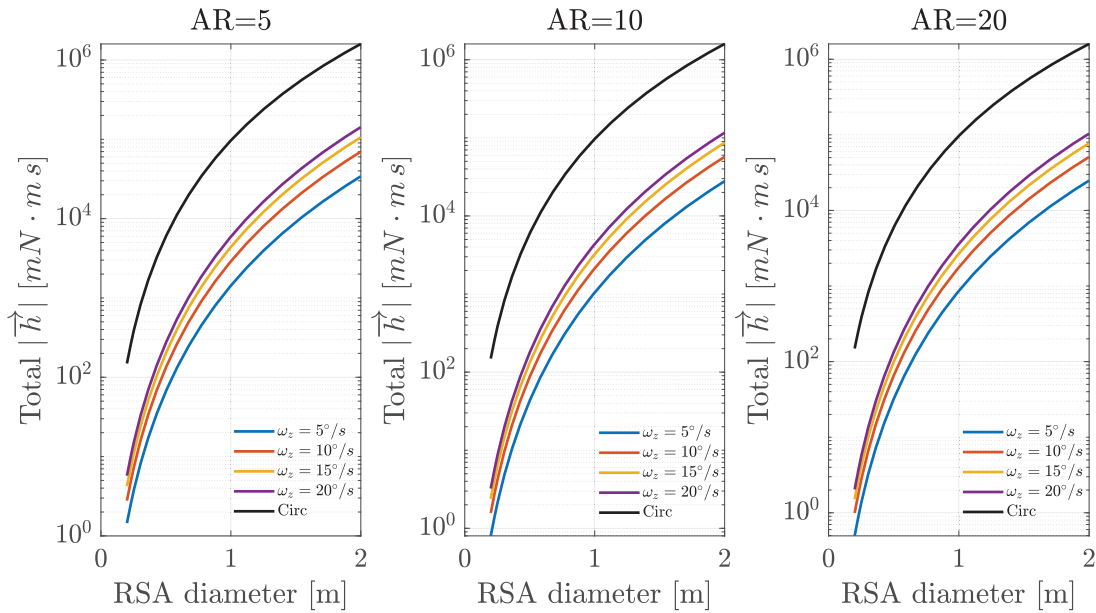


Figure 11. Total angular momentum exchange for an imaging maneuver as a function of aperture diameter.

The Pareto Front was computed using the genetic algorithm and the result is plotted in figure 12. The three axes of the plot correspond to the three objective function discussed in section 3. The cost and total angular momentum exchange axes are plotted on logarithmic scales to ensure all data points are visually discernible from one another given the multiple orders of magnitude present and to be consistent with the respective objective function plots in figures 9 and 11. The Pareto Front for all test cases considered in this work are plotted along with the Pareto Front for a circular aperture design for comparison. The utopia point is located in the foreground where all three objective function values are minimized.

RSA designs with the same aspect ratio are plotted in a single color while the different marker designations correspond to different RSA spin rates. The upper right corner of the plot corresponds to RSA designs that maximize aperture diameter whereas the lower left corner of the plot corresponds to RSA designs that minimize aperture diameter. The Pareto Fronts for each of the test cases had a higher density of solutions in the upper right region of the plot corresponding to larger aperture designs with high cost, high momentum exchange requirements, and high resolution images. Nevertheless, a sufficient number of solutions were found for smaller aperture designs. In order to better visualize the solution set, projections of the Pareto optimal solutions were taken and plotted in 2D. Figure 13 shows the solution set projected in the resolution and cost plane.

The general trend observed is the more costly an OTA is, the higher the resulting image resolution. Given that all variables in Stahl’s cost model were kept constant except for aperture diameter, the increase in OTA cost is solely due to increasing aperture diameter. No correlation is observed between OTA cost and RSA spin rate. However, a decreasing RSA AR does increase OTA cost. The cost increase between adjacent-sized ARs is a factor of 2X for smaller aperture diameters and remains relatively constant as aperture diameter increases. As expected, circular aperture designs cost more than all RSA designs. Compared to circular designs, cost savings for low AR RSAs are up to a factor of 2.5X and 8X for high AR RSAs. From this standpoint, the cost per unit of image resolution is higher for circular aperture designs than it is for RSAs.

Plotting the projection of the solution set onto the resolution and total required angular momentum exchange plane in figure 14, it is clear that the total required angular momentum exchange for circular apertures is higher compared to all RSA test cases considered in this work. For low aspect ratio RSAs, circular apertures require an order of magnitude greater momentum exchange over an observation maneuver whereas two orders of magnitude greater momentum exchange is required for circular apertures compared to high aspect ratio RSAs. Unlike the resolution and cost plane, differences in RSA spin rate is observed to produce different solution sets. RSA test cases with higher spin rates require higher momentum exchange capabilities regardless of AR. RSAs with spin

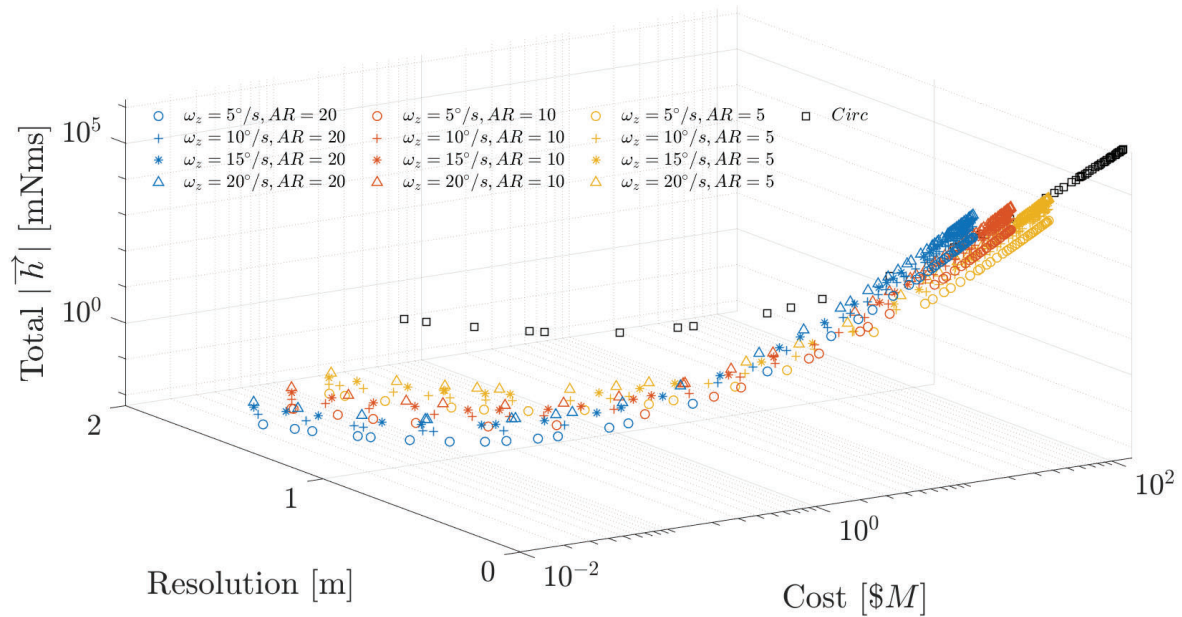


Figure 12. Pareto Frontier for an Earth-observing RSA in a 300km altitude orbit. RSAs with mirror aspect ratios of 5 : 1, 10 : 1, and 20 : 1 and spin rates from 5°/s to 20°/s are plotted.

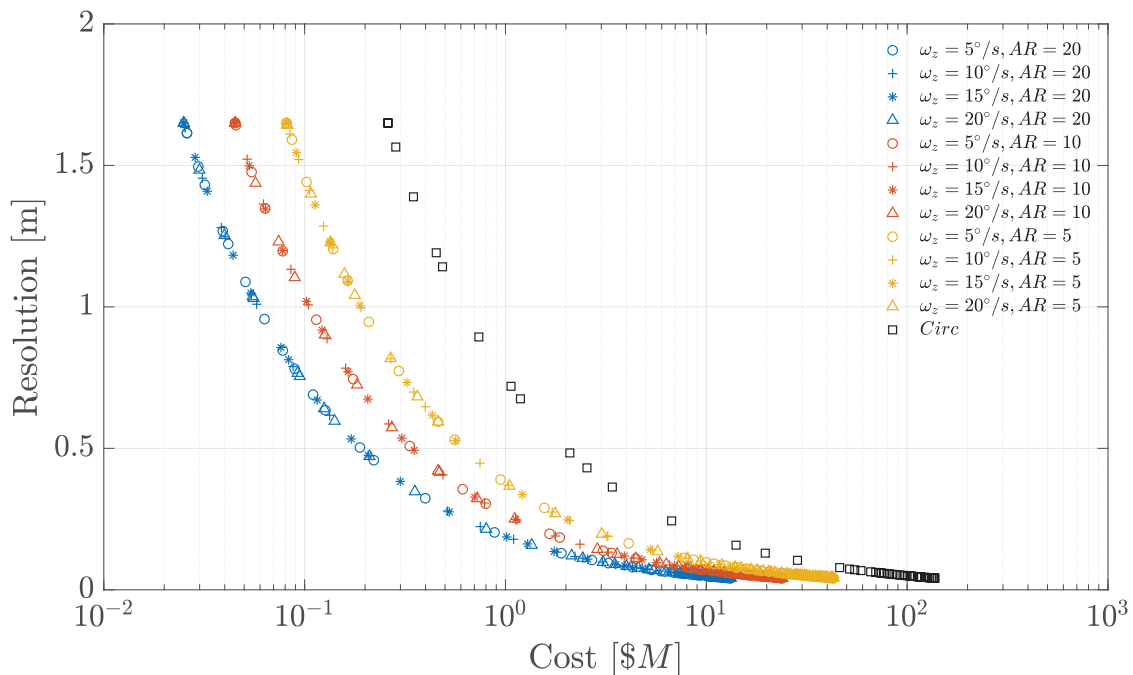


Figure 13. Projection of Pareto Frontier onto OTA cost and image resolution plane.

rates of 5°/s require an order of magnitude less momentum exchange capability compared to spin rates of 20°/s. However, this difference reduces significantly as larger aperture diameter designs are considered as momentum exchange requirements are dominated by the target tracking component of the imaging maneuver as opposed to the spinning component.

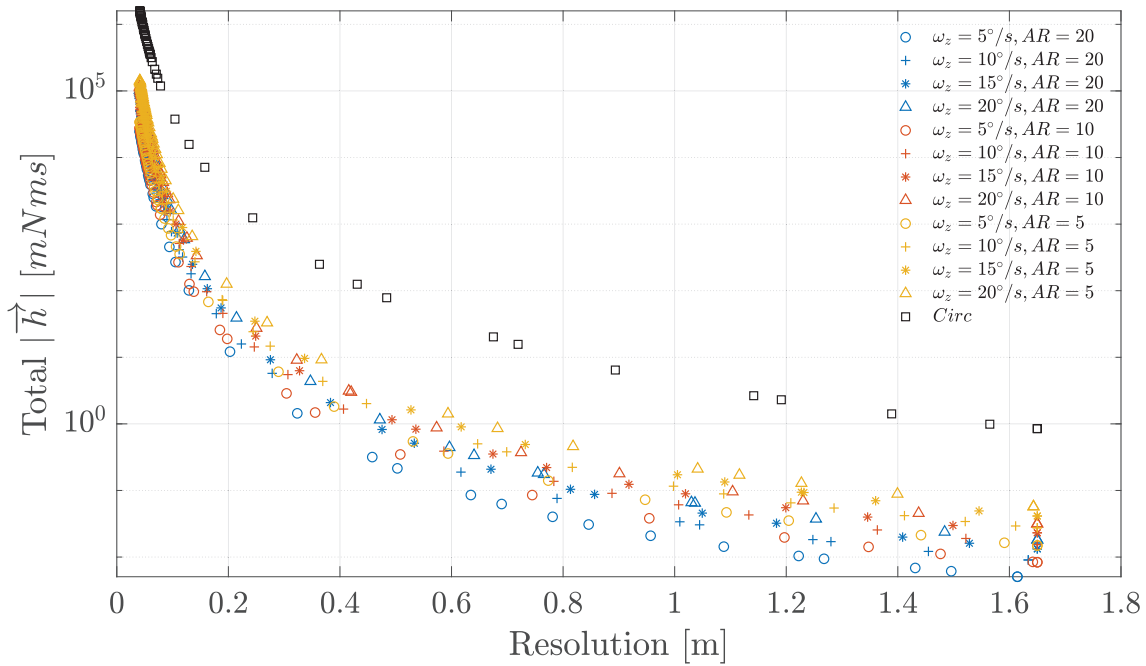


Figure 14. Projection of Pareto Frontier onto image resolution and total angular momentum exchange plane.

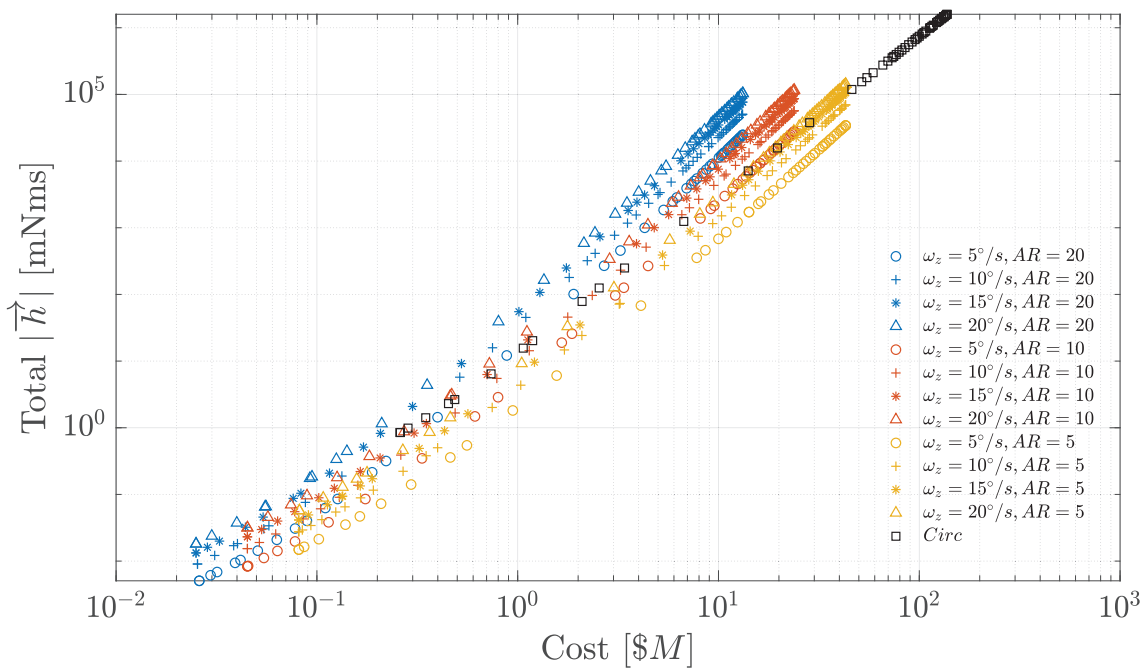


Figure 15. Projection of Pareto Frontier onto OTA cost and total angular momentum exchange plane.

The final projection of the solution set onto the OTA cost and total angular momentum exchange plane in figure 15 shows a general trend of increasing OTA cost to increasing total angular momentum exchange required. This plot suggests that circular aperture designs at a particular price point require less angular momentum exchange. However, all circular aperture points that appear to outperform RSA designs in this

context correspond to smaller aperture diameters compared to the RSA designs. Therefore, this plot should not be used as a comparison between circular aperture and RSA designs as it is misleading in this context. On the other hand, this plot provides useful insight when comparing RSA designs. Understanding of the angular momentum exchange requirements for RSA designs at a particular OTA cost can be read from this plot. This understanding is useful for systems level design of an RSA demonstration mission during which knowledge of the ADCS requirements for various payload costs can drive high level design decisions.

5. DISCUSSION

One of the benefits to using the genetic algorithm for multi objective optimization problems is the ability of the designer to consider a more complete design space compared to algorithms that produce singular value solutions. This enables the solution set to be useful to designers with various application constraints particular to their mission context. For this work, a high level design of an RSA payload for an Earth-orbiting demonstration mission is the mission context. Specifically, a demonstration mission with a large enough aperture to capture imagery with resolution commensurate to the current state of the art, but with OTA cost and ADCS system requirements in the cubesat to small sat regime is desired. Given that this mission context seeks to achieve the most efficient RSA design, the point closest to the utopia point for each test case was plotted in figure 16 along with the corresponding aperture diameter.

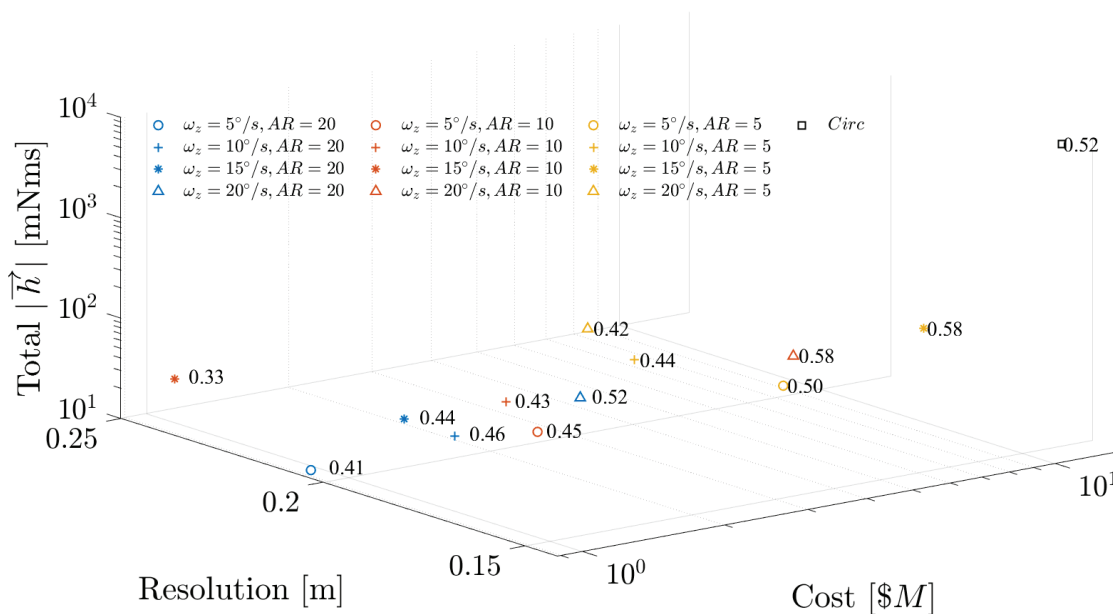


Figure 16. Subset of Pareto Frontier points closest to utopia point with corresponding aperture diameters labeled.

The range of aperture diameters closest to the utopia point is 0.33m to 0.58m. An RSA design within this aperture diameter range and the CMV20000 detector would produce synthesized images with resolutions between 25cm and 14cm, which would rival the current state of the art.¹⁴ This aperture diameter range would enable consideration of a 12U cubesat platform for an RSA demonstration mission assuming each mirror segment, which is half the total diameter in length, would fold along the length dimension of the 12U bus. Angular momentum exchange requirements range from 12mNms to 400mNms. This momentum exchange range is suitable for cubesat and smallsat-scale ADCS. For example, the Blue Canyon Technologies FlexCore ADCS enables 500mNms to 800mNms momentum exchange capacity while occupying roughly 1U of space.

One of the primary considerations in designing an RSA’s sampling strategy is determination of an optimal spin rate. Previous work has bounded the range of acceptable spin rates for RSAs in LEO orbits based on resolution

variation, image smear, and signal to noise ratio (SNR).¹⁴ For a 300km altitude orbit, spin rates between $2^\circ/s$ and $15^\circ/s$ were determined to enable acceptable image capture. The smaller the RSA AR, the greater the number of images required to fully sample the telescope's optical transfer function. The need to capture a greater number of images reduces the maximum exposure time for each image captured in the sequence. This does not have a significant impact on image SNR for Earth observation since the SNR is on the order of 10^6 for individual frame exposure times of 4ms to 10ms.¹⁴

6. CONCLUSION AND NEXT STEPS

In this paper, a multi objective optimization was performed for several RSA payload designs. Three objective functions were defined that, from a high level, characterize the performance and requirements for an RSA mission. The objective functions considered were cost of the OTA, synthesized image resolution, and total angular momentum exchange throughout an imaging maneuver. RSA aperture diameter was varied from $0.2m$ to $2m$ and the genetic algorithm was implemented to obtain a Pareto Front for RSAs with length to width mirror aspect ratios of $5 : 1$, $10 : 1$, and $20 : 1$. The Pareto optimal solutions were analyzed with regard to each objective function axis and compared to a Pareto Front of traditional circular aperture designs. The benefits to RSA designs compared to traditional circular apertures were clearly demonstrated in the result analyses. For the context of an RSA demonstration mission on the cubesat or smallsat scale, a subset of the Pareto optimal solution set closest to the utopia point was discussed. Aperture dimensions for this subset of points, which ranged from $0.33m$ to $0.58m$, may be used as a design point of departure for more detailed RSA demonstration mission designs. A brief discussion on AR effects on RSA sampling strategies was provided.

Next steps for working towards an RSA demonstration mission include the following activities.

1. Develop an analytical expression for the number of frames required to fully sample the telescope's optical transfer function for variable AR designs.
2. Compare total angular momentum exchange requirements presented in this paper with experimentally collected results from the Dynamics and Controls Testbed in the MIT Space Systems Laboratory. Add resulting knowledge of difference between modeled and experimental values to Pareto Front analysis.
3. Perform scalability analysis for larger RSA designs intended for astrophysics applications in terms of required ADCS capabilities and whether current technologies can meet these needs.

ACKNOWLEDGMENTS

The author would like to thank the NASA Space and Earth Sciences office for providing financial support for this work through Astrophysics Analysis and Research grant number 80NSSC20K040. Additionally, the author would like to thank Alejandro Cabrales Hernandez for insightful discussions on RSA dynamics topics covered in this work.

REFERENCES

- [1] Contreras, J. W. and Lightsey, P. A., "Optical design and analysis of the james webb space telescope: optical telescope element," in [*Novel Optical Systems Design and Optimization VII*], **5524**, 30–41, International Society for Optics and Photonics (2004).
- [2] Class, . S. S. E., "Rectangular earth-imaging fast-spinning aperture telescope," tech. rep., MIT (2018).
- [3] Hecht, E., [*Optics*], Pearson Education, Inc., Boston, 5 ed. ed. (2017 - 2017).
- [4] Fiete, R. D., [*The Story of Q*], 109–127, SPIE. <https://www.spiedigitallibrary.org/ebooks/TT/Modeling-the-Imaging-Chain-of-Digital-Cameras/8/The-Story-of-Q/10.1117/3.868276.ch8>.
- [5] Cochrane, A., Schulz, K., Kendrick, R., and Bell, R., "Q selection for an electro-optical earth imaging system: theoretical and experimental results," *Optics express* **21**(19), 22124–22138 (2013).
- [6] Wronski, B., Garcia-Dorado, I., Ernst, M., Kelly, D., Krainin, M., Liang, C.-K., Levoy, M., and Milanfar, P., "Handheld multi-frame super-resolution," *ACM Transactions on Graphics (TOG)* **38**(4), 1–18 (2019).

- [7] Robinson, D. and Milanfar, P., “Statistical performance analysis of super-resolution,” *IEEE Transactions on Image Processing* **15**(6), 1413–1428 (2006).
- [8] Meinel, A. B., “Cost Scaling Laws Applicable To Very Large Optical Telescopes,” in [*Instrumentation in Astronomy III*], Crawford, D. L., ed., **0172**, 2 – 7, International Society for Optics and Photonics, SPIE (1979).
- [9] Meinel, A. B., “Cost relationships for nonconventional telescope structural configurations,” *J. Opt. Soc. Am.* **72**, 14–20 (Jan 1982).
- [10] van Belle, G. T., Meinel, A. B., and Meinel, M. P., “The scaling relationship between telescope cost and aperture size for very large telescopes,” in [*SPIE Astronomical Telescopes + Instrumentation*], (2004).
- [11] Stahl, H. P., “Multivariable parametric cost model for ground and space telescope assemblies,” *Bulletin of the AAS* **51** (9 2019). <https://baas.aas.org/pub/2020n7i143>.
- [12] Maki, J., Gruel, D., McKinney, C., Ravine, M., Morales, M., Lee, D., Willson, R., Copley-Woods, D., Valvo, M., Goodsall, T., et al., “The mars 2020 engineering cameras and microphone on the perseverance rover: A next-generation imaging system for mars exploration,” *Space science reviews* **216**(8), 1–48 (2020).
- [13] McKinney, C., Goodsall, T., Hoenk, M., Shelton, J., Rumney, K., Basset, C., Jeganathan, M., and Moore, D., “Context cameras for the orbiting carbon observatory 3 (oco-3) instrument,” in [*2018 IEEE Aerospace Conference*], 1–15, IEEE (2018).
- [14] Kramer, E. L., *Towards the Advancement of Rotating Synthetic Aperture Space Telescope Technology*, Master’s thesis, Massachusetts Institute of Technology (May 2022).
- [15] Graf, B., “Quaternions and dynamics,” *arXiv preprint arXiv:0811.2889* (2008).
- [16] Chipperfield, A. and Fleming, P., “The matlab genetic algorithm toolbox,” (1995).